Iranian Journal of Chemical Engineering

Journal Homepage: www.ijche.com

pISSN: 1735-5397
eISSN: 2008-2355

Atomistic Molecular Dynamics Simulation of Pyridinium Bromide Ionic Liquids: Quantitative Insights into the Effects of Alkyl Chain Length on Ion Transport and Microstructure

Zahra Fakhri *, ***Azim Soltanabadi***

Faculty of Chemistry, Razi University, Kermanshah, Iran

ARTICLE INFO

Article type:
Research article

Article history:
Received: 2026-02-15
Revised: 2026-03-10
Accepted: 2026-03-25
Available online: 2026-03-27

Keywords:
Pyridinium-based ionic liquids,
RDF,
Heats of vaporization,
Diffusion coefficient

ABSTRACT

This study employs classical molecular dynamics simulations using the OPLS-AA force field to systematically investigate the influence of the length of alkyl chain on the structural, thermodynamic, and dynamical properties of a homologous series of pyridinium-based ionic liquids (methyl- to pentyl-pyridinium bromide). The main objective is to elucidate how the gradual elongation of the alkyl chain affects intermolecular interactions and ion transport behavior at the molecular level. The model demonstrates good agreement with available experimental density data, confirming its reliability for predicting physicochemical trends in these systems. The results indicate that increasing the length of the alkyl chain weakens electrostatic interactions and enhances free volume, leading to a systematic reduction in density and cohesive energy density. The structural analysis reveals well-defined cation–anion coordination shells, reflecting strong local ionic organization across all systems. The dynamical analysis shows a consistent decrease in the ionic mobility with the elongationof chains, due to stronger van der Waals interactions and steric effects, which in turn reduce diffusion and ionic conductivity. Importantly, the ionic transference numbers calculated from ion mobilities clearly demonstrate that cations contribute more to charge transport than anions in all investigated systems. This cation-dominated transport behavior provides a direct molecular-level explanation for the observed decrease in ionic conductivity by increasing the length of chains.

DOI: 10.22034/ijche.2026.572366.1584 URL: https://www.ijche.com/article_245046.html

*Corresponding author: Z.fakhri@razi.ac.ir

1. Introduction

One of the major contributors to environmental pollution is solvent waste, which contaminates both the atmosphere and groundwater systems [1–4]. A substantial fraction of these solvents is consumed in the pharmaceutical industry, significantly contributing to the greenhouse gas emissions associated with chemical manufacturing processes [5,6]. Consequently, the development of environmentally benign solvents has become increasingly important within the framework of green chemistry.

Ionic liquids (ILs) have attracted considerable attention as alternative green solvents because of their unique physicochemical properties, including negligible vapor pressure, excellent thermal stability, high ionic conductivity, and tunable solvation characteristics. These features make ILs attractive for numerous applications such as producing low-toxicity electrolytes, catalysis, extraction, electrochemical technologies, pharmaceutical processes, gas separation, polymerization, and energy storage systems [7–16]. Furthermore, ILs are often referred to as “designer solvents” because their physicochemical properties can be tailored through the structural modification of both the cationic and anionic components [17].

Among the various classes of ionic liquids, alkyl pyridinium bromides have attracted growing interest because of their facile synthesis, simple purification procedures, and versatile physicochemical behavior. These ionic liquids have found applications in extraction and separation technologies, catalysis, electrochemical systems, and materials science. In particular, their tunable hydrophobicity and strong ionic interactions make them promising candidates for anion exchange membranes used in selective ion separation processes such as electrodialysis [18–20].

Despite their advantages, the experimental characterization of ionic liquids remains challenging because their physicochemical properties are highly sensitive to impurities such as water and residual halide ions. Even trace impurities can significantly alter intermolecular interactions, leading to substantial changes in viscosity, conductivity, density, and thermal stability [21]. Therefore, molecular dynamics (MD) simulations have become increasingly important for investigating the microscopic structure, thermodynamics, and transport properties of ionic liquids under a broad range of conditions. Compared with experimental approaches, MD simulations provide molecular-level insight while reducing experimental costs and time requirements and enabling the rational design of ionic liquids with tailored properties [22].

Previous MD studies have demonstrated that the length of the alkyl chain and the anion type strongly influence the viscosity, ionic conductivity, diffusion behavior, and structural organization in ionic liquid systems [21, 22]. However, despite extensive investigations, a comprehensive molecular-level framework correlating the length of the alkyl chain with the coupled structural organization, thermodynamic stability, and transport behavior of pyridinium-based bromide ionic liquids is still lacking. In particular, systematic comparative studies, capable of directly linking the nanoscale structural heterogeneity with macroscopic thermodynamic and transport properties across homologous pyridinium bromide series, remain relatively scarce.

In the present work, this gap is addressed through the comprehensive MD investigation of a homologous series of 1-alkyl-pyridinium bromide ionic liquids ranging from methyl- to pentyl-substituted systems (C1–C5). The novelty of the present study lies in the investigation of structural, thermodynamic,

and dynamic properties within a unified simulation framework. Radial distribution functions (RDFs), velocity autocorrelation functions (VACFs), density, molar volume, enthalpy of vaporization, cohesive energy density, molar heat capacity, and self-diffusion coefficients were systematically analyzed to establish direct relationships between ion–ion spatial organization and macroscopic transport behavior. Furthermore, the influence of the elongation of the alkyl chain on free volume, electrostatic interactions, and dispersion-induced structural organization was quantitatively evaluated to provide deeper mechanistic insight into how density, ion mobility, and ionic conductivity are governed by molecular-scale interactions in pyridinium-based ionic liquids. By establishing these structure–property correlations, the present study provides a molecular interpretation of pyridinium bromide ionic liquids and offers valuable guidance for the rational design of ionic liquids with suitable physicochemical properties for industrial and technological applications.

2. Method

2.1 Simulation details

MD simulations were carried out for the IL systems of 1-alkyl pyridinium bromide $[R_nPy]^+[Br]^-$ (n=1-5) using the DL_POLY 2.20 software package [23]. Each cubic simulation box consisted of 200 ion pairs, and the initial configurations were generated by placing ions randomly. The geometry of isolated ions was optimized at the B3LYP/6-31+G* [24-26] level using Gaussian 09 [27], and a schematic representation of the optimized structures of $[R_nPy]^+[Br]^-$ are shown in Fig. 1. All ions were described using the Optimized Potentials for Liquid Simulations – All Atom (OPLS-AA) force field proposed by Jorgensen et al. [28]. Controlling temperature and pressure was managed through the Nosé–Hoover [29] thermostat and barostat, with relaxation times set to 0.1 ps and 2 ps respectively. The equations of motion were integrated using the Verlet [30] leapfrog method with a timestep of 1 fs. For accurate calculation of long-range Coulombic interactions, the Ewald summation technique [30] with a real-space cutoff explicitly set to 14 Å, was used. Lennard-Jones interactions were truncated at the same cutoff distance of 14 Å. To ensure a smooth decay of the Lennard-Jones potential, a switching function was applied between 12 Å and 14 Å. Periodic boundary conditions (PBC) were applied in all three spatial directions to maintain bulk-like conditions and to mimic an infinite system, thereby eliminating surface effects and artificial interfaces. This approach ensures that the simulated system accurately represents bulk behavior. Long-range electrostatic interactions were calculated using the Ewald summation method, which takes into account interactions with all periodic images. In addition, a sufficiently large cutoff distance (14 Å) was employed, together with an suitably sized simulation box (200 ion pairs), to reduce finite-size effects and ensure the reliability of the calculated properties. No external driving force was applied in this study, and all simulations were performed under equilibrium conditions. The system dynamics are governed solely by interatomic forces derived from the employed force field. No tail corrections were applied to the van der Waals energy and pressure. An NPT production run with a purity of 500 ps was performed at 400 K to calculate the density. To investigate temperature-dependent properties, simulations were conducted at five temperatures: 298.15, 303.15, 308.15, 313.15, and 318.15 K. At each temperature, following a 200 ps equilibration period, three independent 1 ns NVT production runs were carried out. The initial configurations for the NVT runs were taken from the balanced

structures of the previous NPT simulations, ensuring the accuracy and reliability of the calculated properties. This structured simulation protocol provides comprehensive insight into the physicochemical properties of ionic liquids under different thermodynamic conditions.

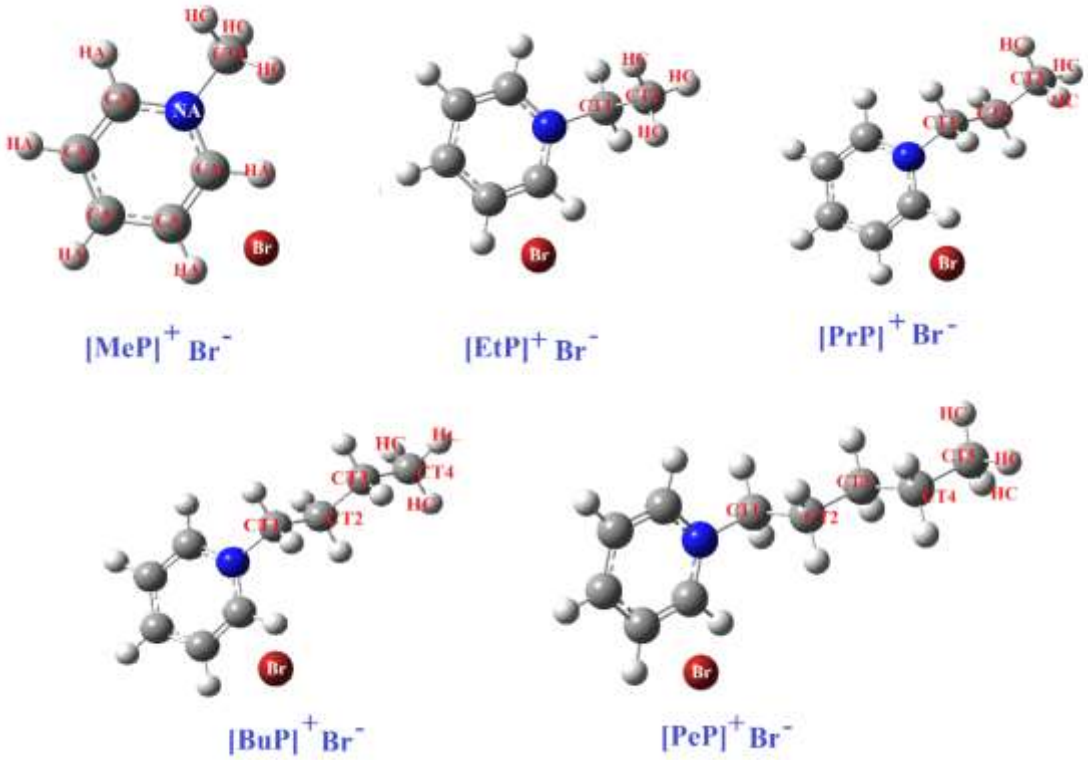

Figure 1. Schematic representation of the structure of pyridinium-based ionic liquids.

2.2 Force field

In this study, the modeling of intramolecular and intermolecular interactions was performed using the classical OPLS-AA force field. The inherent limitations of nonpolarizable force fields, particularly their tendency to underestimate diffusion coefficients due to the absence of explicit electronic polarization effects, should be taken into account. Although employing polarizable force fields and charge-scaling methods can result in obtaining more accurate transport properties of ionic liquids, their high computational cost restricts their use in large-scale and long simulations. The selection of OPLS-AA was based on its proven reliability in reproducing the structural and thermophysical properties of ionic liquid systems, especially those involving alkyl chains and heterocyclic cations. This force field provides an optimal balance between computational efficiency and predictive accuracy, which is crucial for large-scale and long-term molecular dynamics simulations. A force field consists of a mathematical functional form describing the potential energy surface together with a set of associated parameters.

$$U = \sum_{\text{bonds}} K_r (r - r_0)^2 + \sum_{\text{angles}} K_\theta (\theta - \theta_0)^2 + \sum_{\text{dihedrals}} K_\chi [1 + \cos(n\chi - \delta)] + \sum_{i<j} 4\varepsilon_{ij} \left[\left(\frac{\sigma_{ij}}{r_{ij}}\right)^{12} - \left(\frac{\sigma_{ij}}{r_{ij}}\right)^{6} \right] + \sum_{i<j} \frac{q_i q_j}{r_{ij}} \quad (1)$$

In this model, r_0 and θ_0 represent equilibrium structural parameters, while K_r, K_θ and K_χ are force constants. The multiplicity is denoted by $n\chi$ and δ is the phase angle for torsional parameters. The total potential energy of the ionic systems is expressed as the sum of the bonded interactions (harmonic bond stretching, angle bending, and torsional terms represented by cosine series) and non-bonded interactions, including Lennard-Jones (12–6) and Coulombic potentials. Parameters for the $[R_nPy]^+$ cation are adapted from the studies of Liu et al. [30], and for the Br^- anion from those of Lopes and Padua [31]. Nonbonded interactions between atoms, separated by three bonds (1–4 interactions), were scaled by a factor of ½ for both electrostatic and van der Waals terms, while 1–5 electrostatic interactions were scaled by a factor of 1/1.2. All nonbonded interactions between, atoms separated by more than three bonds, were fully included without scaling. The Lorentz-Berthelot combination rules, $\varepsilon_{ij} = \sqrt{\varepsilon_{ii}\varepsilon_{jj}}$ and $\sigma_{ij} = (\sigma_{ii} + \sigma_{jj})/2$ apply to the Lennard-Jones parameters, and the partial charges for the $[R_nPy]^+$ cations are taken from those of Liu et al.'s [30]. The intramolecular and intermolecular parameters used in this study are provided in the Supplementary Information along with the corresponding reference.

It is worth noting that the OPLS-AA used in this study does not include explicit hydrogen atoms; rather, hydrogens are incorporated into their neighboring carbon or nitrogen atoms as united atoms. This approach reduces the computational cost while maintaining reliable accuracy in describing ionic liquids. The schematic structures shown in Fig. 1 represent the optimized geometries of ions but do not explicitly display hydrogen atoms as separate entities.

3. Results and discussion

3.1 Density, molar volume and thermal expansion coefficients

MD simulations have become powerful tools for investigating the properties of ionic liquids (ILs), as direct experimental measurements can be challenging due to their complex physicochemical nature. The choice of interatomic potential models, such as OPLS-AA, is crucial for accurate results and allows for the study of ion interactions and structural properties. MD simulations provide insights into how structural variations, such as changes in the length of the alkyl chain in cations, affect the properties such as density and cohesive energy, aiding in the optimization of ILs for applications in energy storage devices, electrolyte systems, and separation processes. The results often align closely with experimental data, demonstrating the effectiveness of MD in analyzing the thermodynamic and structural behavior of ILs. In this study, the density of $[R_nPy]^+Br^-$ was evaluated using a 500 ps production run performed in the NPT ensemble. The OPLS-AA approach was employed to calculate the density of the ionic liquid at various temperatures. The simulated density values are presented in Table 1. Reliable experimental data for the direct comparison of density values over a broad temperature range, particularly for the investigated pyridinium bromide ionic liquids, remain relatively limited in the literature. Therefore, only two reliable literature sources were identified for the comparison and validation of the simulation results. These data correspond to propyl- and butyl-pyridinium bromide systems with the mole fractions close to unity. The variation of density as a function of

temperature for pyridinium-based ionic liquids, with different lengths of alkyl chains, is illustrated in Fig. 2.

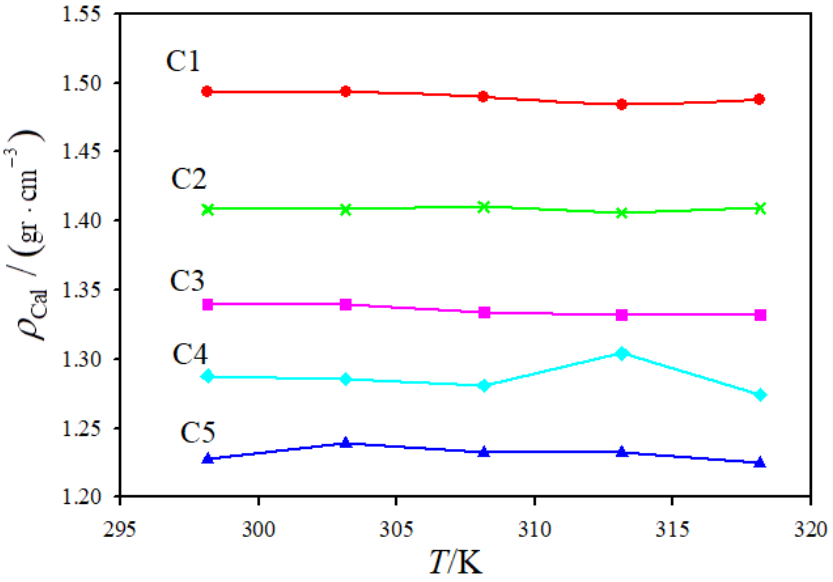

Figure 2. Variation of the calculated density $\rho_{Cal}/(gr\cdot cm^{-3})$ as a function of temperature ,T, for pyridinium-based ionic liquids with the different lengths of alkyl chains (Cn, n = 1 to 5) at 1 atm.

Also, the thermal expansion coefficients (α) of the ionic liquids from fitting the linear variation of $\ln\rho$ with T ($-ln\,\rho = a + \alpha T$) were calculated, and the obtained values are systematically presented in Table 1.

Table 1.

Simulated densities, $\rho_{Cal}/(gr\cdot cm^{-3})$, experimental densities $\rho_{Exp}/(gr\cdot cm^{-3})$ at 298.15K and at 1 atm, with the percent error in densities, $E_\rho\%$, and the thermal expansion coefficients , α , for $[R_nPy]^+Br^-$ ILs.

ILs	$\rho_{Cal}/(gr\cdot cm^{-3})$	$\rho_{Exp}/(gr\cdot cm^{-3})$	$E_\rho\%$	$10^3\alpha/K^{-1}$
$[MeP]^+Br^-$	1.3418			0.2648
$[EtP]^+Br^-$	1.2575			0.4918
$[PrP]^+Br^-$	1.0701	1.0402 [32]	2.8	0.3641
$[BuP]^+Br^-$	1.0362	1.018424 [33]	1.7	0.1382
$[PeP]^+Br^-$	1.0172			0.1971

Standard uncertainties, *u*, are $u(T) = 3K, u(\rho_{Cal}) = \pm 7\times10^{-4}\,gr\cdot cm^{-3}$

The calculation of molar volume, which is obtained from the ratio of the volume of the ionic liquid in question to the number of moles of that liquid, will be discussed next. The changes in the molar volume of $[R_nPy]^+Br^-$: $[MePy]^+Br^-$, $[EtPy]^+Br^-$, $[PrPy]^+Br^-$, $[BuPy]^+Br^-$, and $[PePy]^+Br^-$ at different temperatures, presented in Table 2, Fig. 3, show that the molar volume increases with temperature.

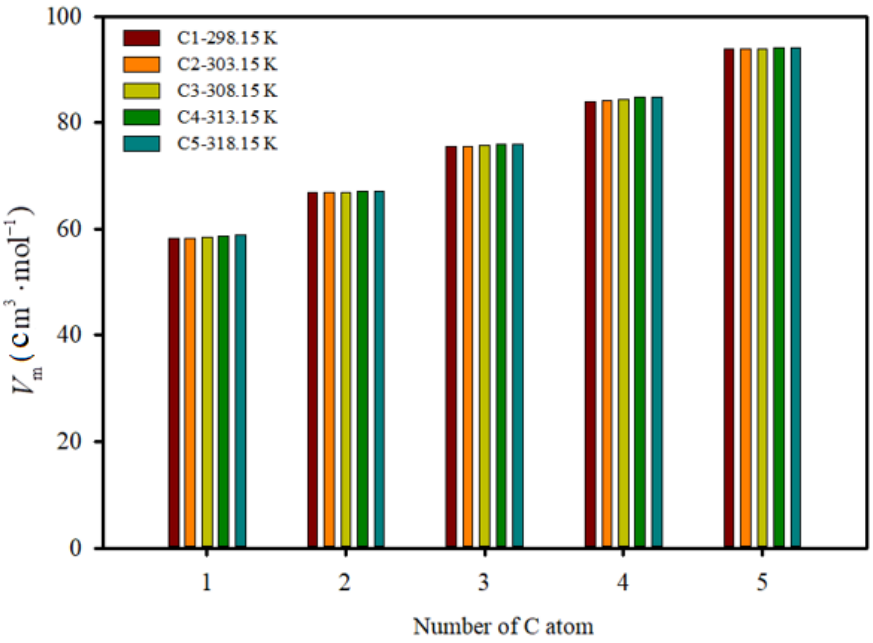

Figure 3. Variation in the molar volume $V_m(m^3 \cdot \text{mol}^{-1})$ as a function of the length of alkyl chains (C_n, n = 1 to 5) in pyridinium-based ionic liquids at different temperatures and 1 atm pressure.

The molar volume of ionic liquids with longer cations, such as $[PePy]^+Br^-$, is higher than that of shorter cations, like $[MePy]^+Br^-$, due to hydrophobic effects and stronger intermolecular interactions. The changes in the molar volume with temperature are minor, indicating the moderate expansion of ionic liquids by increasing temperature. These findings can serve as a solid basis for evaluating and optimizing the properties of ionic liquids for various applications, such as energy storage and electrolyte systems.

Table 2.
Molar volume for $[R_nPy]^+Br^-$ ILs at different temperatures and at 1 atm

ILs	298.15 K	303.15 K	308.15 K	313.15 K	318.15 K	400.15 K
	$V_m(\text{cm}^3 \cdot \text{mol}^{-1})$					
$[MeP]^+Br^-$	58.281	58.321	58.422	58.627	58.794	59.808
$[EtP]^+Br^-$	66.866	66.889	66.970	66.982	67.166	68.073
$[PrP]^+Br^-$	75.402	75.417	75.733	75.873	75.877	76.148
$[BuP]^+Br^-$	83.908	84.061	84.374	84.854	84.869	85.348
$[PeP]^+Br^-$	93.741	93.884	93.897	93.992	93.998	94.650

3.2 Molar vaporization enthalpy, cohesive energy density and molar heat capacity

This section focuses on the calculation of vaporization enthalpy, ΔH_{Vap}, and cohesive energy density, c,. Both properties can be utilized to understand the thermodynamic behavior and intermolecular interactions of ionic liquids.

$$\Delta H_{\text{Vap}} = RT - (U_{int} - U_{ionpair}) \quad (2)$$

where, ΔH_{Vap}, is the molar vaporization enthalpy change at temperatures T and R is the

gas constant. U_{int} is the intermolecular energy of the liquid which can be obtained from the simulation. $U_{ion\,pair}$ represents the average intermolecular energy of an ion pair in the ideal gas state, which can be simulated by a single ion pair at the same temperature in a large enough box. Equation 2 shows the energy difference between the ideal gas state, $U_{ion\,pair}$, and the liquid phase, U_{int}, that plays a crucial role in determining, ΔH_{Vap}. Essentially, this difference represents the amount of the energy required to overcome the intermolecular forces in the liquid. The molar vaporization enthalpy of $[R_nPy]^+Br^-$ ILs ($[MePy]^+Br^-$, $[EtPy]^+Br^-$, $[PrPy]^+Br^-$, $[BuPy]^+Br^-$, and $[PePy]^+Br^-$), listed in Table 3 and Fig. 4, decreases from 298.15 K to 400.15 K, indicating the expected behavior of liquids responding to an increase in temperature. However, the molar evaporation enthalpy is higher for ionic liquids with longer cations compared to those with shorter cations, reflecting stronger intermolecular interactions and a greater energy requirement for evaporation. This trend is attributed to enhanced van der Waals forces and hydrophobic effects in longer cations. At higher temperatures, the decrease in evaporation enthalpy is lower for longer cationic liquids due to the greater difficulty of breaking these bonds and evaporating. Additionally, there is a possibility of the aggregation of alkyl chains and the formation of non-polar domains or nanoscale heterogeneity in ionic liquids with longer cations, which could impact their evaporation properties.

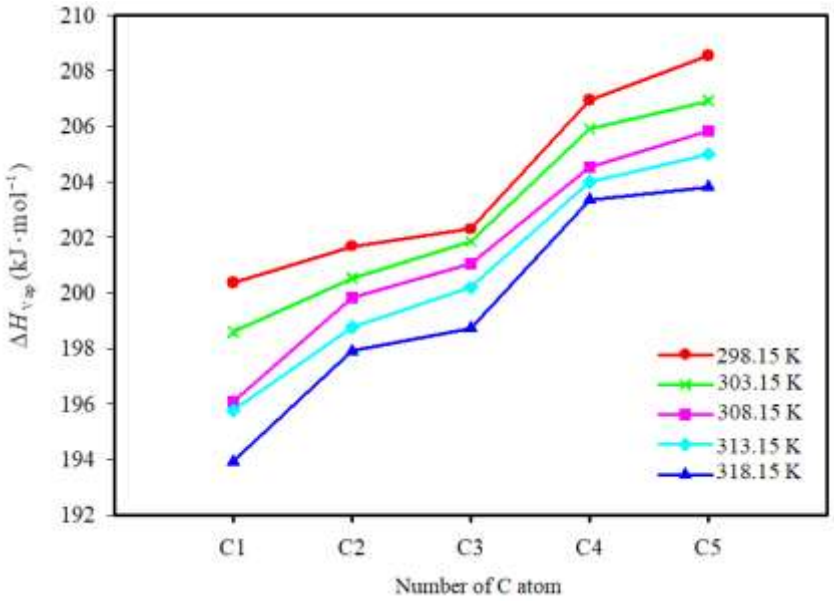

Figure 4. Variation in the enthalpy of vaporization $\Delta H_{Vap}(\mathrm{kJ \cdot mol^{-1}})$ as a function of the length of alkyl chains (C_n, n = 1 to 5) in pyridinium-based ionic liquids at different temperatures and 1 atm pressure.

The cohesive energy density (CED), c, is a measure of the energy needed to overcome intermolecular interactions within a unit volume of a substance. The greater the cohesive energy density, the more adhesive the material is, and the stronger the intermolecular forces become. The cohesive energy density is a measure of the strength of intermolecular interactions in liquids and is calculated using the following equation:

$$c = (U_{int} - U_{ionpair})/V_m \quad (3)$$

$$c = (\Delta H_{Vap} - RT)/V_m \quad (4)$$

c, reflects the intermolecular forces in the liquid phase and explains the liquid's thermodynamic and structural properties. This parameter significantly impacts the physical properties of liquids, solids, and solutions and is important in materials science, chemistry, and biology. Cohesive energy quantifies the strength and extent of these forces that maintain the density and structure of liquids, aiding in the design of materials with specific properties. An increase in the energy difference between the ideal gas state and the liquid state indicates the higher c. These simulated values at different temperatures and at 1 atm are reported in Table 4. Also, the changes of c, are shown in Fig. 5.

Table 3.
Molar vaporization enthalpy, ΔH_{Vap}, for $[R_nPy]^+Br^-$ ILs at different temperatures and at 1 atm.

ILs	298.15 K	303.15 K	308.15 K	313.15 K	318.15 K	400.15 K
	$\Delta H_{\mathrm{Vap}}(\mathrm{kJ \cdot mol^{-1}})$					
$[MeP]^+Br^-$	200.371	198.591	196.086	195.756	193.921	180.301
$[EtP]^+Br^-$	201.676	200.531	199.827	198.756	197.895	181.586
$[PrP]^+Br^-$	202.303	201.854	201.074	200.203	198.712	183.423
$[BuP]^+Br^-$	206.954	205.913	204.556	204.013	203.348	184.725
$[PeP]^+Br^-$	208.549	206.922	205.833	205.007	203.824	186.910

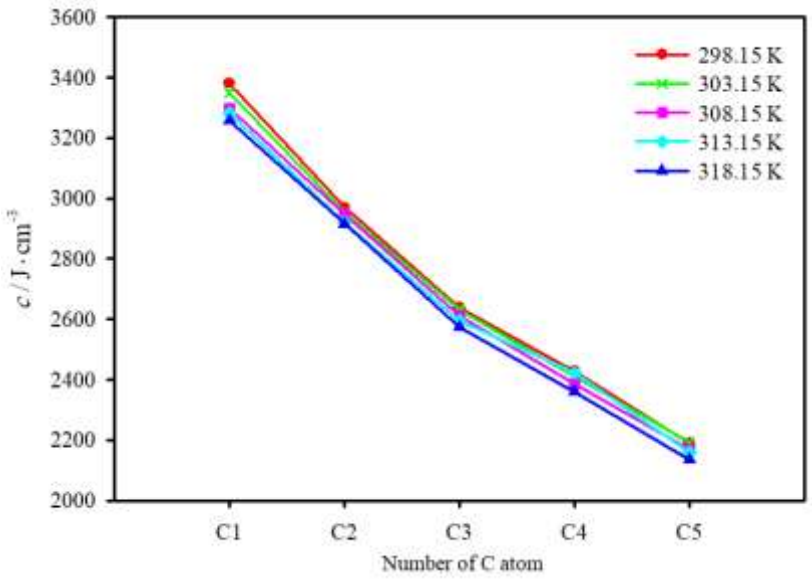

Figure 5. Variation in the cohesive energy density (CED, $c/J \cdot \mathrm{cm}^{-3}$) as a function of the length of alkyl chains (C_n, n = 1 to 5) in pyridinium-based ionic liquids at different temperatures and 1 atm pressure.

Both increasing temperature and the elongation of the alkyl chains reduce the cohesive energy density (CED) of ionic liquids, although through different mechanisms. At higher temperatures, the enhanced molecular motion and increased intermolecular distances weaken the overall intermolecular interactions, thereby

decreasing the CED. In contrast, the elongation of alkyl chains increases the molar volume, causing the intermolecular cohesive energy to be distributed over a larger volume. Consequently, although the total intermolecular energy becomes more negative by increasing the length of alkyl chains, indicating stronger cohesive interactions, the CED decreases because of the dominant volumetric effect.

Table 4.
Cohesive energy density, c, for $[R_nPy]^+Br^-$ ILs at different temperatures and at 1 atm.

ILs	298.15 K	303.15 K	308.15 K	313.15 K	318.15 K	400.15 K
			$c/J \cdot cm^{-3}$			
$[MeP]^+Br^-$	3380.940	3350.398	3299.408	3282.260	3258.321	2921.426
$[EtP]^+Br^-$	2970.809	2953.660	2947.367	2922.003	2916.348	2211.032
$[PrP]^+Br^-$	2638.355	2632.401	2611.117	2594.820	2575.016	2027.547
$[BuP]^+Br^-$	2426.793	2409.977	2384.953	2422.150	2358.478	1929.087
$[PeP]^+Br^-$	2189.233	2191.936	2168.232	2159.492	2134.135	1727.480

At the end, the calculation of the molar heat capacity, C_p, (from the slope of the enthalpy of ILs with respect to temperature T) was performed. These values are reported in Table 5. These changes are shown in Fig. 6. The, C_p, of ILs increases from $[MePy]^+Br^-$ to $[PePy]^+Br^-$ as the alkyl chain lengthens. This rise is due to more atoms and greater degrees of freedom, allowing higher thermal energy storage. However, the rate of increase decreases with longer chains, as they have a diminished impact on the thermal degrees of freedom. Shorter chains exhibit stronger electrostatic interactions, while longer chains show greater hydrophobic effects. This trend highlights the crucial role of the length of chains in the thermodynamic behavior and thermal stability of ionic liquids.

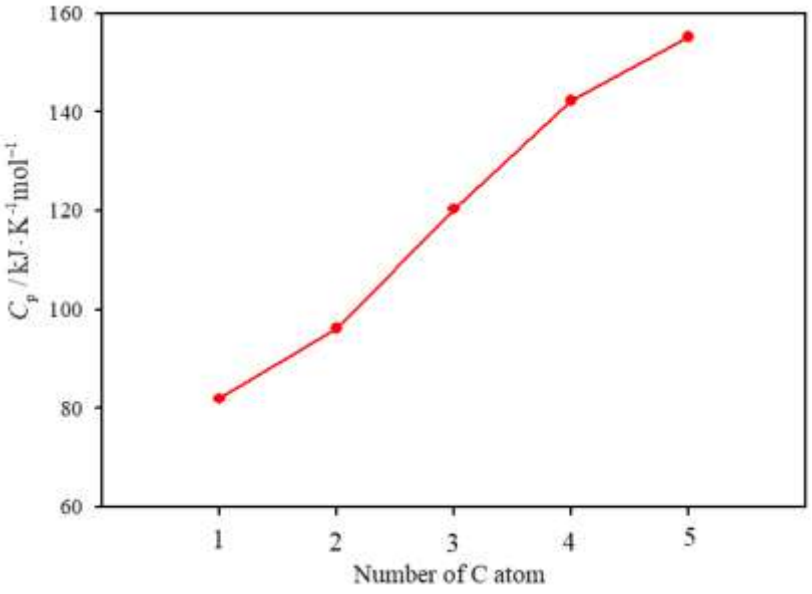

Figure 6. Variation in the molar heat capacity $C_p/\mathrm{kJ} \cdot K^{-1}\mathrm{mol}^{-1}$ as a function of the length of alkyl chains (C_n, n = 1 to 5) in pyridinium-based ionic liquids at different temperatures and 1 atm pressure.

Table 5.
Molar heat capacity for $[R_nPy]^+Br^-$ ILs at different temperatures and at 1 atm.

ILs	$C_p/\mathrm{kJ}\cdot K^{-1}\mathrm{mol}^{-1}$
$[MeP]^+Br^-$	81.9
$[EtP]^+Br^-$	96.04
$[PrP]^+Br^-$	120.36
$[BuP]^+Br^-$	142.32
$[PeP]^+Br^-$	155.14

3. 3 Microscopic structure and RDF

The radial distribution function (RDF) is a widely used structural analysis tool for characterizing the microscopic organization of fluids [34,35]. It describes the probability of finding particles at a given distance from a reference particle and provides important information regarding short-range ordering, intermolecular correlations, and local structural arrangements in complex systems such as ionic liquids. The RDF analysis is particularly useful for examining how structural variations, including alkyl chain elongation, influence the molecular organization and ion–ion interactions within the system.

Using the Center of ring (CR) as the reference point provides a more accurate and reliable depiction of cation structure due to its geometrical rigidity and insensitivity to alkyl chain fluctuations. In contrast, the center of mass is prone to artifacts caused by the movement of flexible side chains.

The RDF for CR of pyridinium -Br^- reveals two distinct peaks for the bromine anion interacting with the pyridinium ring, as exhibited in Fig. 7a. The first sharp peak indicates a close interaction between the bromine anion and the nitrogen atom of the pyridinium ring, leading to the aggregation of alkyl chains and the formation of non-polar domains or nanoscale heterogeneity at smaller radii. These interactions are electrostatic in nature, where the positively charged nitrogen interacts strongly with the negatively charged bromine anion, stabilizing the initial aggregation. This behavior is consistent with nanosegregation [36-38], referring to the nanoscale separation into polar and apolar domains within the ionic liquid. As the distance increases, the second, broader peak emerges, reflecting hydrophobic interactions between the alkyl chains. These hydrophobic interactions facilitate the organization and stabilization of alkyl chain aggregates, promoting the formation of more ordered nanoscale domains.

By increasing the length of alkyl chains, the size and stability of hydrophobic aggregates increase, as indicated by the shift in the second peak. This behavior is consistent with nanosegregation, i.e., the formation of distinct polar and apolar domains at the nanoscale, which plays a key role in determining the microstructure and properties of liquids. Shorter chains, like methyl, tend to form smaller, less stable aggregates, whereas longer chains, such as pentyl, promote the formation of larger and more stable hydrophobic domains due to enhanced hydrophobic interactions. The bromide anion exhibits a clear preference for interacting with the pyridinium nitrogen rather than the alkyl groups. This preference is due to the electrostatic nature of the nitrogen in the pyridinium ring, which creates a positive charge that attracts the negatively charged bromide anion. These interactions help stabilize the central core of the aggregates. The combination of this interaction with the length of the alkyl chains, which dictates the stability and size of these aggregates, plays a crucial role in designing ionic liquids with specific properties.

The analysis of the RDF of N-Br for $[R_nPy]^+Br^-$ with varying lengths of alkyl chains, as shown in Fig. 7b, reveals that the peak intensities in RDF are significantly

influenced by the length of alkyl chains. The peaks for longer alkyl chains, such as pentyl, exhibit higher intensities, indicating stronger hydrophobic interactions and the formation of larger, more stable alkyl chain aggregates. These more intense peaks correspond to the enhanced hydrophobic interactions at larger distances and stronger electrostatic interactions between the bromide anion and pyridinium nitrogen. In contrast, shorter chains like methyl, ethyl, and propyl lead to smaller and less stable aggregates, with correspondingly weaker RDF peaks. The RDF peaks near zero represent closer interactions between the bromide anion and the pyridinium nitrogen, which stabilize the central core of the aggregates. At larger radii, the hydrophobic interactions between the alkyl chains dominate, leading to the formation and stabilization of these aggregates. Additionally, the bromide anion has a greater affinity for interacting with the nitrogen in the pyridinium ring rather than the alkyl chains, helping to stabilize the aggregate core. Overall, this study emphasizes the critical roles of the length of alkyl chains and the electrostatic properties of the bromide anion in the formation and stability of aggregates. These findings are vital for the design and optimization of ionic liquids for applications in catalysis, drug delivery systems, and non-polar material transport.

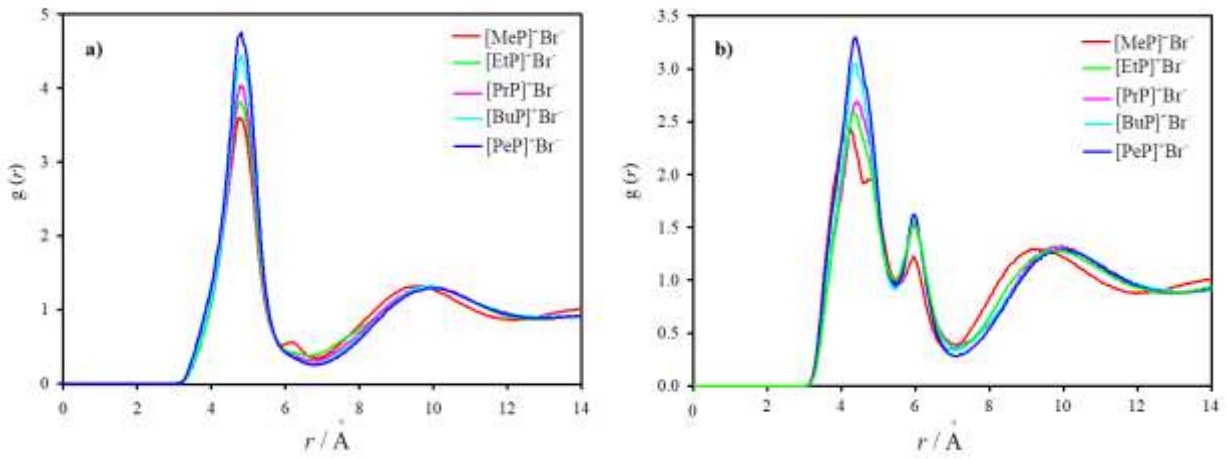

Figure 7. (a) RDFs for the center of the ring (CR) for cation–anion interactions, and (b) N-Br interactions for pyridinium-based ionic liquids at 400 K and 1 atm.

Fig. 8a shows the RDFs for cation-cation interactions using CR as the reference point, revealing two distinct peaks. The first, sharp and pronounced peak corresponds to the first coordination shell, where strong electrostatic and van der Waals interactions organize cations into a well-defined, densely packed structure at short distances. The second peak, broader and less intense, represents the second coordination shell, reflecting less ordered and more dynamic cation arrangements at longer distances. This peak highlights the effects of molecular mobility and increased hydrophobicity on the liquid structure beyond the immediate coordination environment.

In propylpyridinium, the first peak is notably sharper and higher than the same in other ionic liquids, indicating a more compact and stable cation network. This is attributed to the optimal length of alkyl chains, which balances flexibility and steric hindrance, resulting in stronger electrostatic and dispersion interactions. Conversely, longer alkyl chains, such as butyl and pentyl, exhibit broader and

lower peaks, indicating reduced structural order and cation proximity due to enhanced hydrophobic effects. This leads to decreased packing density and weakened structural correlations.

As shown in Fig. 8b, the RDF of Br-Br for $[R_nPy]^+Br^-$ ILs suggest that anions have a strong preference for interacting with the nitrogen atom in the pyridinium ring, rather than the alkyl chains. This preference is driven by the electrostatic interactions between the negatively charged bromide anion and the positively charged nitrogen. In systems with shorter alkyl chains, such as methyl, the RDF peaks are sharper and more concentrated, indicating tighter and more organized interactions between the bromide anions and the nitrogen. These interactions lead to the stabilization of the aggregate core. In contrast, for systems with longer alkyl chains, such as pentyl, the hydrophobic interactions between the alkyl groups become more prominent, causing a reduction in the order of the anion-anion interactions and resulting in broader and weaker RDF peaks. This suggests that longer alkyl chains disrupt the close packing of bromide anions around the pyridinium nitrogen, weakening the electrostatic interactions and leading to a more disordered structure.

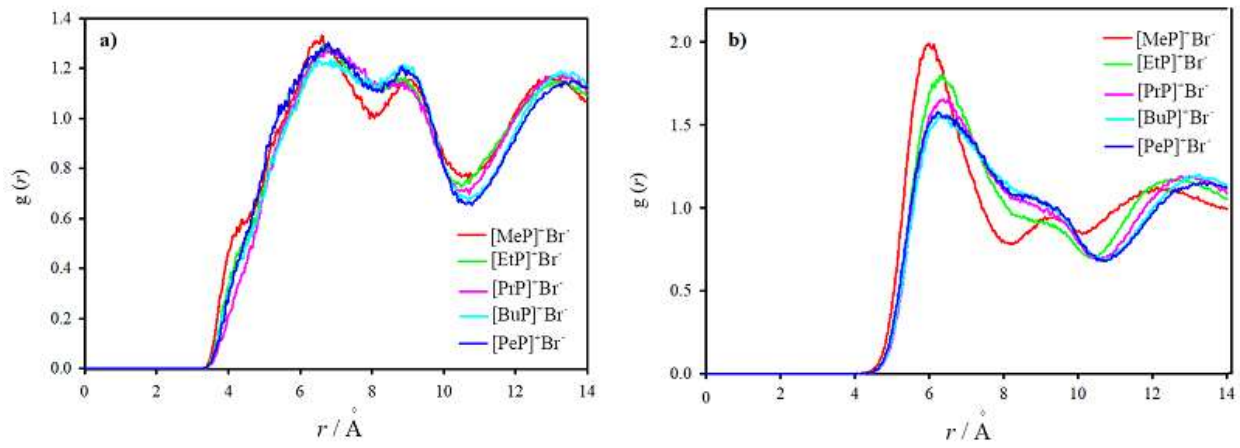

Figure 8. RDFs for (a) the center of ring (CR) of cation–cation interactions, (b) anion– anion interactions for pyridinium-based ionic liquids at 400 K and 1 atm.

3.4 Velocity Autocorrelation Function (VACF)

The enhancement of the ionic conductivity in ionic liquids can be achieved by facilitating ion mobility through reducing the cage effect, shortening velocity randomization times, and optimizing cation–anion interactions. In general, ions with lower effective mass and bulkier alkyl substituents tend to exhibit weaker electrostatic interactions and reduced transient ion trapping, thereby promoting ionic transport. Furthermore, the selection of cation–anion combinations with weaker intermolecular interactions and faster velocity relaxation dynamics can contribute to improved ionic conductivity. These factors play an important role in the rational design of ionic liquids for electrochemical applications such as batteries and fuel cells.

The normalized Velocity Autocorrelation Function, $C_{v,i}(t)$, is a mathematical tool derived from MD simulations. It quantifies the temporal correlation of the velocity of the center of mass of a specific ion, *i*, in the system [39]. It is expressed as:

$$C_{v,i}(t) = \frac{\langle V_i^c(t) V_i^c(0) \rangle}{\langle V_i^c(0) V_i^c(0) \rangle} \quad (5)$$

$C_{v,i}(t)$ measures the correlation between the velocity of the ion at time *t* and its initial velocity at *t*=0, averaged over all possible starting points in time, indicated by ⟨ ⟩. $V_i^c(t)$ denotes the velocity of the center of mass of the ion at time *t*. This normalized function provides insights into the dynamical behavior of ions, such as their mobility and interaction with the surrounding environment. VACF is particularly important as it connects the microscopic motion of particles to macroscopic transport properties. By analyzing the decay of VACF, one can gain a deeper understanding of ionic motion, collisional processes, and cage effects within a system, especially in complex fluids like ionic liquids. For the calculation of VACFs, three independent 1 ns NVT simulations were carried out at each temperature. Initial configurations were taken from well-separated snapshots of the equilibrated 500 ps NPT trajectory to ensure statistical independence and reproducibility. In Figs.7a, b, the calculated VACF is plotted for both cations and anions at 400K and at 1.0 atm.

In the Fig. 9a, for the cations ($[MePy]^+$, $[EtPy]^+$, $[PrPy]^+$, $[BuPy]^+$, $[PePy]^+$), the first zero in VACF occurs within the range of 0.15 to 0.2 ps, indicating the mean collision time. As the length of alkyl chains increases from $[MePy]^+$ to $[PePy]^+$, this time slightly increases. After the first zero, VACF enters negative values, representing the cage effect, which persists for approximately 0.2 to 0.4 ps. The cage effect is more pronounced and stable for the heavier cations. At longer times, beyond 0.4 ps, VACF approaches zero as the velocities randomize. Lighter cations, such as $[MePy]^+$, equilibrate faster, while heavier cations, such as $[PePy]^+$, exhibit slower velocity relaxation.

In the Fig. 9b, for the bromide anion (Br^-), the first zero in VACF occurs at approximately 0.2 ps, representing its mean collision time. Unlike for the cations, the VACF for bromide decreases more rapidly and reaches negative values sooner. The cage effect for the anion occurs within a shorter range, approximately 0.2 to 0.3 ps, and with less intensity compared to that for the cations. This behavior suggests that the bromide anion has greater mobility and escapes its local cage environment more quickly. After 0.3 ps, the VACF for bromide rapidly approaches zero, indicating faster velocity randomization and a shorter relaxation time compared to the same for cations.

In the final comparison between cations and the bromide anion, the mean collision time for the lighter cations is shorter (~0.15 ps) and increases to around 0.2 ps as the length of alkyl chains grows. The bromide anion has a mean collision time similar to the heavier cations but displays a faster decrease in its VACF. The cage effect lasts longer and is more intense for the cations, extending up to approximately 0.4 ps, whereas for the bromide anion, it ends around 0.3 ps. Ultimately, the velocity of the heavier cations, particularly $[PePy]^+$, relaxes more slowly, while the bromide anion randomizes its velocity more quickly and reaches equilibrium faster.

The dynamic concepts discussed in this topic can be used to optimize thermodynamic properties and electrical conductivity [36].

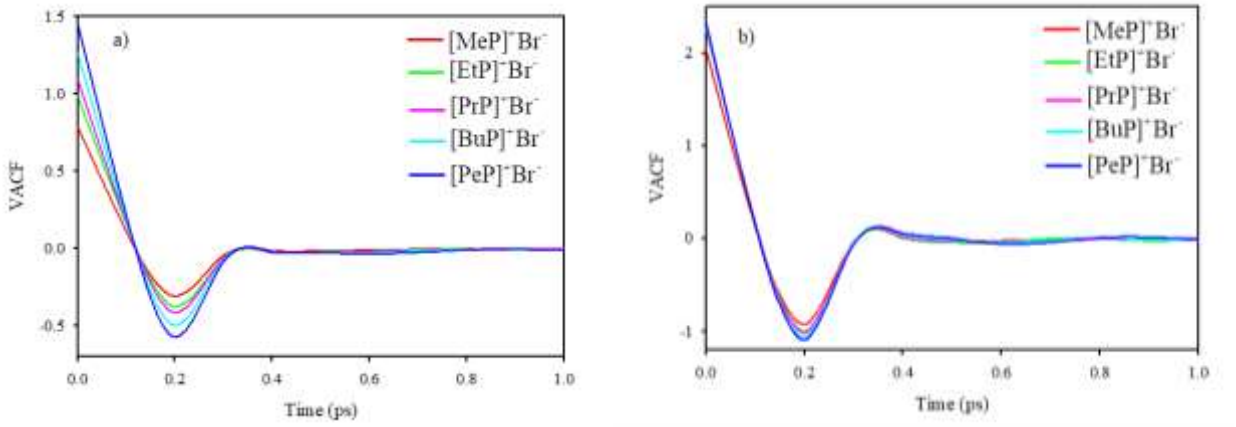

Figure 9. VACF curves normalized for the cation (a) and the anion (b) for pyridinium-based ionic liquids within an NVT ensemble at 400 K and 1 atm.

3.5 MSD and Self-diffusion coefficient and ionic conductivity

The mobility of ions in ionic liquids (ILs) is commonly characterized using two important dynamic properties: MSD and diffusion coefficients [40]. Among these, the self-diffusion coefficient provides direct insight into the random thermal motion of individual ions within the liquid medium. This coefficient is typically determined from the slope of MSD as a function of time after the system reaches the diffusive regime. Unlike thermodynamic properties, which are primarily equilibrium-based, the self-diffusion coefficient is inherently dynamic and therefore requires time-dependent approaches such as MD simulations. One of the major challenges in studying ionic liquids is identifying an appropriate simulation time scale for reliable diffusion calculations, since ion pairing and strong interionic interactions can significantly influence ion mobility. Nevertheless, the Einstein relation remains a well-established and reliable framework for evaluating self-diffusion coefficients in condensed-phase systems.

$$D_i = \frac{1}{6} \lim_{t\to\infty} \frac{d}{dt} \left\langle \left[\vec{r}_i(t) - \vec{r}_i(0)\right]^2 \right\rangle \qquad (6)$$

In the above equation, the quantity in braces represents the ensemble-averaged MSDs of the molecules over time t, with $\vec{r}_i$ denoting the position vector of the center of mass of ion i. MSDs were calculated from the NVT simulations for five ILs, and the averages for the centers of mass of both cations and anions at 400 K and at 1.0 atm up to 1 ns are shown in Figs. 8a, b.

Table 6.

Diffusion coefficient, D, of cations and anions for $[R_nPy]^+Br^-$ ILs from the slope of MSD plots, and cationic and anionic transference numbers at 400K and 1 atm.

ILs	$D_+/10^{-11}m^2/s$	$D_-/10^{-11}m^2/s$	t_+	t_-	$\sigma/S \cdot m^{-1}$
$[MePy]^+Br^-$	0.685	0.408	0.626	0.373	0.164
$[EtPy]^+Br^-$	1.085	0.675	0.138	0.861	0.299
$[PrPy]^+Br^-$	1.334	1.332	0.500	0.499	0.465
$[BuPy]^+Br^-$	1.553	1.394	0.527	0.473	0.525
$[PePy]^+Br^-$	0.766	0.391	0.662	0.337	0.197

In Fig. 10a, the MSD analysis shows that the cations with longer alkyl chains, such as $[BuPy]^+$ and $[PePy]^+$, appear to enter the sub-diffusive (Cage Escape) region and then the diffusive region more quickly. This is likely due to the greater freedom of movement and fewer electrostatic interactions, compared to smaller cations like $[MePy]^+$ and [EtPy]+. For the anions, brought in Fig. 10b, a similar effect seems to be observed. Bromide anions in compounds with longer alkyl chains like $[PePy]^+$ and $[PrPy]^+$ enter the diffusive region faster. While cations with longer alkyl chains enter the diffusive region more quickly, this does not necessarily indicate an overall increase in diffusivity for longer chains. The MSD curve represents the initial dynamic behavior, but the overall diffusion coefficient depends on the data listed in Table 6. The MSD curves for anions and cations in ionic liquids $[RnPy]^+Br^-$ show three key dynamic regions, each providing valuable insights into ionic motion behavior: First, the Ballistic Region is examined. At very short times (sub-picosecond scale ~ < 1 ps), in the ballistic regime, both cations and anions move with nearly constant velocity, as collisions have not yet occurred. This results in free, non-accelerated motion governed by the initial momentum of the ions. Movement in this region is primarily influenced by the initial momentum and short-term interactions with the environment. Cations with longer alkyl chains (e.g., $[PePy]^+$) show less displacement in this region due to their larger mass and fewer interactions with other ions. In contrast, anions, due to their stronger charge and electrostatic interactions with cations, show faster initial motion. The Sub-Diffusive (Cage Escape) Region, typically observed at up to ~1-50 ps, is when ions encounter the "cage" formed by electrostatic and van der Waals interactions with their surroundings. Cations and anions with longer alkyl chains (like $[BuPy]^+$ and $[PePy]^+$) escape the cage faster due to fewer hydrophobic interactions and more space to move. Smaller cations ($[MePy]^+$ and $[EtPy]^+$) remain in this region longer due to stronger interactions with the environment. In the Diffusive Region, occurring at longer times, ions exhibit free diffusion. Larger cations like $[BuPy]^+$ and $[PePy]^+$ reach this region faster because the formation of alkyl chain aggregates reduces electrostatic interactions with the anions. Anions in compounds with shorter alkyl chains, such as $[MePy]^+$ and $[EtPy]^+$, enter this region more slowly. The diffusivity values for cations (D_+) and anions (D_-) are provided in Table 6. Cation diffusivity initially increases with the length of alkyl chains (from $[MePy]^+$ to $[BuPy]^+$), peaking at $[BuPy]^+Br^-$, but decreases in $[PePy]^+Br^-$. This decrease is likely attributed to enhanced hydrophobic interactions and the resulting aggregation of alkyl chains. For anions, the highest diffusivity is observed in $[PrPy]^+Br^-$, but decreases for longer chains. This reduction results from the restricted anion mobility caused by the formation of hydrophobic domains. Table 6 shows the cation (t_+) and anion (t_-) transfer numbers. t_+ increases in longer alkyl chains, while t_- decreases, indicating the reduced anion involvement in charge transfer. Longer alkyl chains in cations (like $[PePy]^+$) enhance hydrophobic interactions and promote the formation of alkyl chain aggregates, which decrease the overall diffusivity of both cations and anions. This results in faster entry into the diffusive region for cations like $[PePy]^+$ but reduced ion mobility and lower anion transfer numbers, limiting the contribution of anions to charge conduction.

In shorter alkyl chains (like $[MePy]^+$), stronger electrostatic interactions reduce the mobility and charge transfer of both cations and anions.

In longer alkyl chains (like $[PePy]^+$), the formation of nanoscale aggregates reduces overall diffusivity but increases the contribution of cations cations to charge transfer. In compounds with longer chains, hydrophobic effects and nanoscale aggregation play the most significant role in reducing ion mobility. In cations D_+, by increasing the lenghth of alkyl chains from $[MePy]^+$ to $[BuPy]^+$, cation diffusivity increases and peaks at $[BuPy]^+Br^-$ (1.553Å). In $[PePy]^+Br^-$, diffusivity decreases to 0.766. This reduction is due to stronger hydrophobic interactions and the formation of more stable hydrophobic clusters, which limit the movement of cations. In anions D_-, the highest diffusivity is observed in $[PrPy]^+Br^-$ (1.332Å), but it decreases in longer alkyl chains like $[BuPy]^+$ and $[PePy]^+$. This decrease is due to the formation of hydrophobic clusters by longer-chain cations, which trap the anions in a more restricted environment. These findings suggest that tuning the length of alkyl chains and ionic structure can optimize transport properties in ionic liquids, providing valuable insights for material design and industrial applications.

The apparent simultaneous observation of an earlier onset of the diffusive regime and a reduction in diffusivity for longer alkyl chains suggests the presence of two distinct dynamical processes operating on different time scales. The faster transition to the diffusive regime is associated with a more rapid decay of the short-time ballistic and sub-diffusive motion, which arises from the enhanced local structural disorder and increased conformational flexibility of the elongated alkyl side chains. This facilitates the quicker relaxation of velocity correlations at short times. In contrast, the long-time diffusive behavior is governed by collective intermolecular interactions and spatial constraints within the ionic network. In this regime, increasing the length of alkyl chains strengthens van der Waals interactions and promotes steric hindrance and nanoscale aggregation, which collectively restrict the long-range translational motion of ions. Consequently, although longer chains exhibit faster relaxation into the diffusive regime, their overall mobility is reduced. This clearly demonstrates that the onset of diffusion and the magnitude of diffusivity are controlled by different physical mechanisms and should not be interpreted as contradictory trends.

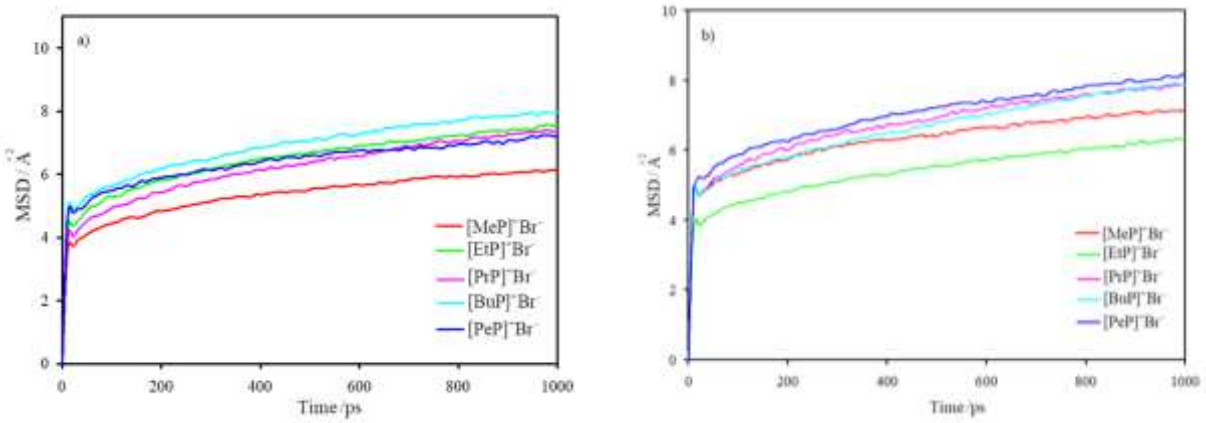

Figure 10. MSDs for the cation (a) and the anion (b) in pyridinium-based ionic liquids within an NVT ensemble at 400 K and 1 atm.

To complement the microscopic diffusion analysis, we estimated the ionic conductivity ,σ, of the studied ionic liquids using the Nernst-Einstein equation:

$$\sigma = \frac{e^2}{V k_B T}(N_+ D_+ + N_- D_-) \qquad (7)$$

where e is the elementary charge, V is the system volume, k_B is the Boltzmann's constant, T is the absolute temperature, and $N_\pm$ and $D_\pm$ denote the number and diffusion coefficients of cations and anions respectively. Based on the data presented in Table 6, the ,σ, of $[RnPy]^+Br^-$ ionic liquids at 400 K is evidently influenced by the length of the alkyl chain of the cation. The initial increase in conductivity by increasing the length of alkyl chains can be attributed to the enhanced free volume and improved ion mobility, facilitating more efficient charge transport. However, a significant decline in conductivity is observed for samples with longer alkyl chains, which is primarily due to increased structural cohesion and dynamic constraints, particularly through the formation of nanoscale aggregates that effectively restrict ionic motion. This behavior reflects a delicate and complex balance between the molecular spatial effects and structural organization, playing a decisive role in the charge transport mechanisms within these complex ionic liquid systems. The absence of charge scaling may affect the absolute magnitude of transport properties; however, since all systems were simulated consistently, the comparative trends across the homologous series remained reliable.

4. Conclusions

In this study, $[R_nPy]^+Br^-$ (n ranges from 1 to 5) ILs were systematically investigated using molecular dynamics simulations, employing a OPLS-AA to ensure the accurate representation of their structural and thermodynamic properties. The length of the alkyl chain of cations is a key determinant of the properties of ionic liquids. Extended chains substantially increase the molar volume and attenuate electrostatic interactions, resulting in significant alterations to both their structural organization and thermodynamic characteristics. Minor changes in molar volume with temperature indicate the thermal stability of these liquids. By increasing temperature and the length of chains, vaporization enthalpy and cohesive energy density decrease, while molar heat capacity increases. These findings highlight the critical role of the length of alkyl chainsin the thermodynamic behavior and thermal stability of ionic liquids.

RDFs were used to investigate the local structure of ionic liquids. The calculations included the center of ring RDFs for various pairs and site–site RDFs. The results showed that increasing the length of the alkyl chain of cations leads to a more ordered and closer first anion shell around the cation. These changes indicate the impact of the length of alkyl chains on intermolecular interactions and the overall liquid structure, which in turn influences the thermodynamic and dynamic properties of ionic liquids. The results from the RDF analyses, alkyl chain aggregation, and thermodynamic behavior collectively indicate nanosegregation in the ionic liquids, characterized by the formation of polar and apolar domains.

The VACF analysis shows that lighter cations, such as [MePy]+, have shorter velocity relaxation and collision times (~0.15 ps), while heavier cations like [PePy]+ exhibit longer collision times (~0.2 ps) and slower velocity randomization. The cage effect is more pronounced and longer-lasting for heavier cations (~0.4 ps), while for the bromide anion (Br^-), it is shorter (~0.3 ps) and less intense, indicating greater mobility. These results

highlight the importance of the size of ions and length of alkyl chains in ionic conductivity, and optimizing these factors can improve performance in the applications such as energy storage and fuel cells.

The MSD analysis and ion diffusivity show that longer alkyl chains accelerate cage escape and ion diffusion, but due to the formation of self-assembled alkyl chain structures and stronger hydrophobic interactions, ion mobility decreases. Cation diffusivity initially increases and peaks at $[BuPy]^+$, but decreases in $[PePy]^+$ due to the restricted movement from more stable nanoscale aggregates. Anion diffusivity also decreases with the length of chains. Optimizing the length of alkyl chains can improve transport properties. The onset of diffusive behavior and the magnitude of diffusivity originate from different dynamical regimes and should not be interpreted as contradictory trends.

OPLS-AA serves as a powerful and reliable framework for accurately simulating and optimizing the thermodynamic properties of ionic liquids. It facilitates the rational design of ionic liquids with superior ionic conductivity, exceptional thermal stability, and optimized transport properties, making them ideal for applications in energy storage and advanced electrochemical systems. This approach lays the groundwork for future research into more complex systems, driving innovations in cutting-edge technologies such as supercapacitors and lithium-ion batteries.

Acknowledgements

The authors sincerely thank and appreciate the Research Council of Razi University for providing the necessary facilities and support to carry out this research.

References

[1] Ahluwalia VK (2021) Green chemistry: Environmentally benign reactions. Springer Nature. https://doi.org/10.1007/978-3-030-58513-6.

[2] Jiménez-González C, Constable DJ (2011) Green chemistry and engineering: a practical design approach. John Wiley & Sons. ISBN: 978-0-470-17087-8.

[3] Dunn PJ (2012) The importance of green chemistry in process research and development. Chem Soc Rev 41:1452-1461. http://dx.doi.org/10.1039/c1cs15041c.

[4] Sheldon RA (2012) Fundamentals of green chemistry: efficiency in reaction design. Chem Soc Rev 41:1437-1451. http://dx.doi.org/10.1039/c1cs15219j.

[5] Capello C, Fischer U, Hungerbühler K (2007) What is a green solvent? A comprehensive framework for the environmental assessment of solvents. Green Chem 9:927-934. http://dx.doi.org/10.1039/b617536h.

[6] Slater CS, Savelski M (2007) A method to characterize the greenness of solvents used in pharmaceutical manufacture. J Environ Sci Health A 42:1595-1605. http://dx.doi.org/10.1080/10934520701517747.

[7] Imam HT, Krasňan V, Rebroš M, Marr AC (2021) Applications of ionic liquids in whole-cell and isolated enzyme biocatalysis. Molecules 26:4791. https://doi.org/10.3390/molecules26164791.

[8] Bedrov D, Piquemal JP, Borodin O, MacKerell AD Jr, Roux B, Schröder C (2019) Molecular dynamics simulations of ionic liquids and electrolytes using polarizable force fields. Chem Rev 119:7940−7995. http://dx.doi.org/10.1021/acs.chemrev.8b00763.

[9] Begić S, Jónsson E, Chen F, Forsyth M (2017) Molecular dynamics simulations of pyrrolidinium and imidazolium ionic liquids at graphene interfaces. Phys Chem Chem Phys 19:30010-30020. https://doi.org/10.1039/C7CP03389C.

[10] Reddy TDN, Mallik BS (2020) Ionic dynamics of hydroxylammonium ionic liquids: a classical molecular dynamics

simulation study. J Phys Chem B 124:4960-4974. https://doi.org/10.1021/acs.jpcb.0c01388.

[11] Sedghamiz E, Moosavi M (2017) Tricationic ionic liquids: structural and dynamical properties via molecular dynamics simulations. J Phys Chem B 121:1877-1892. https://doi.org/10.1021/acs.jpcb.6b10766.

[12] Zhu X, Mu L, Zhu J, Lu X, Ji Y (2024) The role of hydrogen bonding in solubilizing camptothecin in hydrophilic and hydrophobic ionic liquids. Green Chem Eng 5:489-500. https://doi.org/10.1016/j.gce.2023.12.002.

[13] Liu H, et al. (2012) Thermal and transport properties of six ionic liquids: an experimental and molecular dynamics study. Ind Eng Chem Res 51:7242-7254. https://doi.org/10.1021/ie300222a.

[14] Panbo P, Thubsuang U, Payaka A (2025) Molecular dynamics simulations of hydrogen-bonded network structures of polybenzoxazines in the gas phase and aqueous solution. J Mol Graph Model 134:10883. https://doi.org/10.1016/j.jmgm.2024.108893.

[15] Dhakal P, Das SK, Shah JK (2022) Revealing hydrogen bond dynamics between ion pairs in binary and reciprocal ionic liquid mixtures. J Mol Liq 368:120515. https://doi.org/10.1016/j.molliq.2022.120515.

[16] Fedorova IV, Krestyaninov MA, Safonova LP (2021) Structure and ion-ion interactions in trifluoroacetate-based ionic liquids: quantum chemical and molecular dynamics simulation studies. J Mol Liq 328:115449. https://doi.org/10.1016/j.molliq.2021.115449.

[17] Tong B, Liu QS, Tan ZC, Welz-Biermann U (2010) Thermochemistry of alkyl pyridinium bromide ionic liquids: calorimetric measurements and calculations. J Phys Chem A 114:3782–3787. https://doi.org/10.1021/jp9047538.

[18] Sowmiah S, Esperança JMSS, Rebelo LPN, Afonso CAM (2018) Pyridinium salts: from synthesis to reactivity and applications. Org Chem Front 5:453–493. https://doi.org/10.1039/c7qo00836h.

[19] Zhang Q, He H, Wang H, Zhang Z, Chen C (2019) Efficient catalytic oxidation of methyl aromatic hydrocarbon with N-alkyl pyridinium salts. RSC Adv 9:38891–38896. https://doi.org/10.1039/c9ra08185b.

[20] Yang J, Chen Q, Afsar NU, Ge L, Xu T (2023) Poly (alkyl-biphenyl pyridinium)-Based Anion Exchange Membranes with Alkyl Side Chains Enable High Anion Permselectivity and Monovalent Ion Flux. Membranes 13:188. https://doi.org/10.3390/membranes13020188.

[21] Mahmood Fatemi S, Foroutan M (2015) Recent findings about ionic liquids mixtures obtained by molecular dynamics simulation. Nanostruct Chem 5:243–253. https://doi.org/10.1007/s40097-015-0155-0.

[22] Zhua G, Zhoua S, Maa Z, Xua J (2025) Molecular dynamics simulation of the interaction between ionic liquid [OPy][BF4] and SO2. Fluid Phase Equilib 589:114257. https://doi.org/10.1016/j.fluid.2024.114257

[23] Forester TR, Smith W (1995) DL_POLY. Warrington: CCLRC, Daresbury Laboratory. Available from http://www.stfc.ac.uk/CSE/randd/ccg/software/DL_POLY/25526.aspx.

[24] McLean AD, Chandler GS (1980) Contracted Gaussian basis sets for molecular calculations. I. Second row atoms, Z= 11–18. J Chem Phys 72:5639–5648. http://dx.doi.org/10.1063/1.438980.

[25] Krishnan R, Binkley JS, Seeger R, Pople JA (1980) Self consistent molecular orbital methods. XX. A basis set for correlated wave functions. J Chem Phys 72:650–654. http://dx.doi.org/10.1063/1.438955.

[26] Grimme S, Ehrlich S, Goerigk L (2011) Effect of the damping function in dispersion corrected density functional theory. J Comput Chem 32:1456–1465. https://doi.org/10.1002/jcc.21759.

[27] Frisch MJ, et al. (2009) Gaussian 09, Revision D.01. Gaussian, Inc.: Wallingford, CT.

[28] Jorgensen WL, Maxwell DS, Tirado-Rives J (1996) Development and testing of the OPLS all-atom force field on conformational energetics and properties of organic liquids. J Am Chem Soc 118:11225–11236. https://doi.org/10.1021/ja9621760.

[29] Hoover WG (1985) Canonical dynamics: Equilibrium phase-space distributions. Phys Rev A 31:1695. https://doi.org/10.1103/PhysRevA.31.1695 .

[30] Allen MP, Tildesley DJ (1987) Computer simulation of liquids. Clarendon: Oxford. https://doi.org/10.1093/oso/9780198803195.001.0001.

[31] Fakhri Z, Soltanabadi A (2025) An experimental-computational analysis of molecular interactions and its effect on thermodynamic properties of mixtures of isobutanol and ethylbenzene. Results Chem 15:102286. https://doi.org/10.1016/j.rechem.2025.102286

[32] Meng X, He J, Xu C (2022) Preparation of Ionic Liquid 1-Propylpyridinium Bromide [C3py] Br and the Molar Surface Quasi-Gibbs Energy Model of Its Aqueous Solution. J Chem Eng Data 67:23–27. https://doi.org/10.1021/acs.jced.1c00569.

[33] Shaikh VR, Terdale SS, Gupta GR, Hundiwale DG, Patil KJ (2013) Thermodynamic studies of ionic interactions in aqueous solutions of N-butyl-pyridinium bromide at 298.15 K. J Mol Liq 186:14–22. https://doi.org/10.1016/j.molliq.2013.04.027.

[34] van Leeuwen ME, Smit B (1995) Molecular simulation of the vapor-liquid coexistence curve of methanol. J Phys Chem 99:1831–1833. https://doi.org/10.1021/j100007a006.

[35] Fakhri Z, Soltanabadi A (2024) A Combined Experimental, DFT and Molecular Dynamics Simulation Study of Binary Mixture of Ethylbenzene and Aniline. ChemistrySelect 9:e202401340. https://doi.org/10.1002/slct.202401340.

[36] Soltanabadi A, Fakhri Z (2025) DFT study of 1, 4-diazabicyclo [2.2. 2] octane (DABCO) based ionic liquids: Effect of alkyl chain and anion types. Results Chem 15:102285. https://doi.org/10.1016/j.rechem.2025.102285.

[37] Ferreira ML, Pastoriza-Gallego MJ, Araújo JMM, Canongia Lopes JN, Rebelo LPN, Piñeiro MM, Shimizu K, Pereiro AB (2017) Influence of Nanosegregation on the Phase Behavior of Fluorinated Ionic Liquids. J Phys Chem C 121:5415–5427. https://doi.org/10.1021/acs.jpcc.7b00516.

[38] Shimizu K, et al. (2010) Three commentaries on the nano-segregated structure of ionic liquids. J Mol Struct THEOCHEM 946:70–76. https://doi.org/10.1016/j.theochem.2009.11.034.

[39] Feng G, Chen M, Bi S, Goodwin ZAH, Postnikov EB, Brilliantov N, Urbakh M, Kornyshev AA (2019) Free and bound states of ions in ionic liquids, conductivity, and underscreening paradox. Phys Rev X 9:021024. https://doi.org/10.1103/PhysRevX.9.021024.

[40] Koishi T, Fujikawa S (2010) Static and dynamic properties of ionic liquids. Mol Simul 36:1237–1242. https://doi.org/10.1080/08927020903536358.